Predicting macroscopic plastic flow of high-performance, dual-phase steel through spherical nanoindentation on each microphase

Byoung-Wook Choi
Division of Materials Science and Engineering, Hanyang University, Seoul 133-791, Korea

Dong-Han Seo and Jang-Yong Yoo
Technical Research Laboratories, POSCO, Pohang 790-785, Korea

Jae-il Jang[a)]
Division of Materials Science and Engineering, Hanyang University, Seoul 133-791, Korea

(Received 2 August 2008; accepted 9 October 2008)

An attempt was made to predict the macroscopic plastic flow of a high-performance pipeline steel, consisting of dual constituent phases (soft ferrite and hard bainite), by performing nanoindentation experiments on each microphase with two spherical indenters that have different radii (550 nm and 3.3 μm). The procedure is based on the well known concepts of indentation stress-strain and constraint factor, which make it possible to relate indentation hardness to the plastic flow of the phases. Additional consideration of the indentation size effect for sphere and application of a simple "rule-of-mixture" led us to a reasonably successful estimation of the macroscopic plastic flow of the steel from the microphases properties, which was verified by comparing the predicted stress-strain curve with that directly measured from the conventional tensile test of a bulky sample.

I. INTRODUCTION

In constructing pipelines for transporting natural gas and crucial oil over a long distance, application of higher-strength linepipes has many economical advantages[1] such as the increase in transportation efficiency (which can be achieved by increasing operating pressure) and the reduction in materials costs (by decreasing wall thickness and thus total tonnage of pipeline steel and welding consumables). Accordingly, many efforts have been competitively made to develop and apply higher-grade pipeline steels beyond conventional API X65 steel that have a yield strength of 65 ksi (~450 MPa). Recently, the application of a high-strength linepipe such as API X80 grade have been increased, and API X100 and even X120 grade steels have been considered for practical use in the field.[1–5] One of the most recent challenges in this research area of pipeline engineering is developing advanced steels for new design-concept pipelines (referred to as "strain-based design pipeline") that are applicable to the seismic and permafrost regions where large plastic deformation can be introduced to buried linepipes.[6,7] In addition to high strength, an important requirement for this strain-based design pipeline steel is excellent deformability, namely high work-hardening ability (and thus low yield-to-tensile strength ratio). Because dual-phase microstructures consisting of hard and soft phases are known to have a higher hardenability than single-phase structures,[3,8,9] two types of microstructures have been extensively considered for the high-deformability pipeline steels; ferrite-bainite and bainite-martensite. For such a dual-phase steel, to optimize the volume fraction of each phase is essential to obtain proper target properties. In this regard, some pioneering work was made by Tomota and colleagues,[10–12] who designed a micromechanical way to predict the macroscopic stress-strain relation of dual-phase steels using the flow properties of each phase. Jacques and coworkers[13–15] also proposed various micromechanical approaches to link the phase properties to the mechanical behavior of multiphase steels. In recent studies, Ishikawa et al.[3,4] adopted the micromechanics model to optimize the microstructure (especially volume fraction of each phase) of high-performance, dual-phase pipeline steel. However, in the procedure, there is difficulty in obtaining the flow curve of each constituent phase because conventional tensile or compression tests cannot be applied to such a small volume of the microphase.

One promising technique to overcome this difficulty is load-depth sensing nanoindentation,[16–18] which is widely used to probe mechanical properties (typically hardness H and Young's modulus E) of small volume in a target material. In the past decade, a number of studies have been undertaken to measure the small-scale mechanical properties of microphase in metals and alloys

[a)]Address all correspondence to this author.
e-mail: jijang@hanyang.ac.kr
DOI: 10.1557/JMR.2009.0101

TABLE I. Chemical composition and carbon equivalent (C_{eq}) of the examined API X100 steel.

Elements	C	Si	Mn	P	S	Nb	V	Mo	Ceq
Content (%)	0.05 ∼0.07	0.25	≤2.0	≤0.01	≤0.001	≤0.05	≤0.05	≤0.3	0.46∼0.48

through nanoindentation experiments.[19–24] While a three-sided pyramidal Berkovich indenter was mostly used in the previous studies,[19–24] nanoindentation with a spherical indenter (for which analytical solutions are well known) offers distinct merits[25–28] based on the fact that representative stress and strain underneath the spherical indenter increase as penetration depth increases. However, the increase in representative stress and strain does not occur during a sharp indentation due to the geometrical self-similarity of the tip and it is only possible by varying the indenter angle. Thus, a variety of sharp indenters that have different angles might be needed to estimate the flow properties (for experimental studies, see Refs. 29–32), which makes it difficult to obtain the properties from a single grain of microphase.

With this in mind, in this study we attempted to predict the macroscopic plastic flow behavior of ultrahigh performance pipeline steel that consists of dual phases (ferrite and bainite) through nanoindentation experiments on each constituent phase with two spherical indenters having different radii (550 nm and 3.3 μm). The result was compared with that directly measured from a conventional tensile test of the bulky sample.

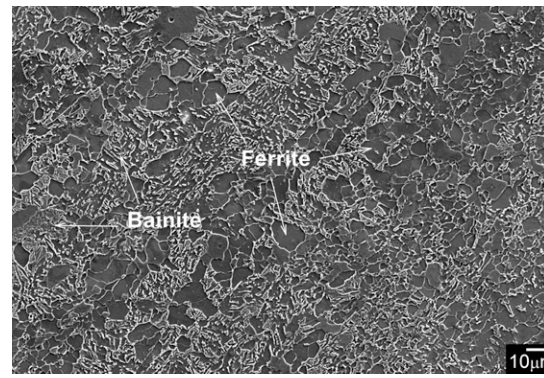

FIG. 1. Scanning electron micrograph showing typical microstructures of API X100 steel examined in this work.

II. EXPERIMENTAL DETAIL

The material examined in this work is API-X100 grade ultrahigh strength pipeline steel fabricated by a thermomechanical-controlled process (TMCP) at POSCO (Pohang, Korea). The chemical composition and carbon equivalent of the steel is listed in Table I. Figure 1 presents a typical scanning electron microscopy (SEM) image of microstructure in the API X100 steel. The material mainly consists of ferrite and bainite phase whose volume fractions, as measured by an image analyzer (Image-Pro; Media Cybernetics Inc., Silver Spring, MD), were approximately 41 and 59%, respectively.

Nanoindentation tests were performed under the continuous stiffness measurement (CSM) module of Nanoindenter-XP (Nano Instruments, Oak Ridge, TN) with two spherical indenters having different radii (commercially quoted as 1 and 5 μm). The real tip radii of the indenters were examined by analyzing the indentations made in fused quartz based on the Herzian contact theory,[33] and they were found to be approximately 550 nm and 3.3 μm, respectively. With these tips, the load-controlled experiments were performed at a constant loading rate of 0.1 mN/s up to the maximum load (P_{max}) of 15 mN for the 550-nm tip and 30 mN for the 3.3-μm tip. More than 5 indentation tests under each testing condition were made on electropolished samples instead of mechanically polished samples to avoid artifacts related to a hardened surface layer. The specimen surface was initially ground with fine emery paper of #2000 and then electrically polished using Lectropol-5 instrument (Struers, Westlake, OH) in a solution appropriate for this steel (butoxy-ethanol 35%, methanol 59%, and perchloric acid 6%) at −30 °C.

After indentation, the specimens was slightly etched in 3% nital acid, and we observed hardness impression and microstructure ex situ within a field-emission SEM, JSM-6330F (JEOL Ltd., Tokyo, Japan) to check out whether indentation was made inside the target microphase. Finally, for comparison purposes the tensile tests of the bulky sample were conducted by using a universal testing machine, Instron 5585 (Instron Inc., Norwood, MA).

III. RESULTS AND DISCUSSION

A. Measuring nanohardness of microphases

There have been numerous efforts to obtain a stress-strain relation from single spherical indentation (for recent studies, see Refs. 34–37). Most of these are based on the well known Tabor's empirical relationship between hardness (H) and representative flow stress (σ):

$$H = \frac{P}{\pi a^2} = C\sigma \quad , \qquad (1)$$

where P is indentation load, a is the radius of contact, and C is constraint factor, whereas the characteristic indentation strain underneath a spherical indenter is often described as

$$\varepsilon = 0.2\frac{a}{R} \quad , \tag{2}$$

where R is the radius of the sphere. Therefore, the first step to estimate the representative flow stress and strain is to experimentally determine a and then H and ε.

Figure 2 shows some representative examples of load-displacement (P-h) curves obtained with 550 nm and 3.3 μm tips. Although P_{max} for R = 3.3 μm is twice that for R = 550 nm, h_{max} for the former is much smaller than that for the latter due to the larger radius of sphere. Unlike a sharp indentation that typically exhibits the relation of $P = Kh^2$ during loading sequence (so-called Kick's law, where K is a constant for curvature), the P-h curve of the loading portion in the figure shows the continuous decrease in the curvature K with increasing penetration depth.

It is very constructive to consider the possible influence of grain size (or grain/phase boundary) on the nanoindentation results. Note that we could not intentionally make an indentation on the target phase, because the tests were made on an electropolished surface. Thus, after etching the indented sample slightly, we observed the hardness impression and microstructure within SEM, which made it possible to select the indentations made near the center of the target microphase (see inset of Fig. 2). By using only the data from selected indentations, we could avoid the grain boundary strengthening effect for ferrite phase having relatively big grain. In the case of bainite where the lath size is small (see inset of Fig. 2), no indentation can be made without hitting lath boundaries. However, the lath boundary is a naturally small angle boundary that does not induce significant boundary strengthening. In Fig. 2, the reproducibility of the testing results is manifested as two curves obtained from the same target phase (but different grain) are overlapped. It should also be noted that for R = 550 nm, only the data points up to the h = 170 nm (over which the spherical shape in the used spheroconical indenter is no longer maintained) were used for analysis, although h_{max} in the experiments was much higher. The reason for making indentation to $h_{max} \gg 170$ nm is to make it easier to observe the location of hardness impression by SEM.

In Fig. 2, for both tips, the ferrite phase exhibits a larger peak-load displacement than the bainite phase, indicating that the former phase is much softer than the latter phase. To estimate the hardness change with indentation depth, first the contact depth (h_c) was determined in a manner outlined by Oliver and Pharr[16,17]:

$$h_c = h - \omega\frac{P}{S} \quad , \tag{3}$$

where S is the contact stiffness (which is the same as the initial slope of unloading curve) and ω is a geometric constant (0.75 for a sphere).[16,17] Then, in consideration of the contact geometry, the radius of contact (a) was calculated as[21]:

$$a^2 = 2Rh_c - h_c^{\,2} \quad , \tag{4}$$

and the mean pressure under the contact, p_{m} (which is equal to the indentation hardness H), was obtained by Eq. (1). Note that the materials pile-up possibly occurring around the contact was not considered here, because the way to quantitatively describe the phenomenon has not been fully established.

Figure 3 summarizes the variation in hardness as a function of normalized indentation depth (h/h_{max}). It should be noted that the data points at very early stage of contact were not used in this study due to a large fluctuation in the data. Also, for R = 550 nm, hardness values are provided only for the range $h \leq 170$ nm, where the spherical geometry holds valid. One can find two tendencies in the figure: first, for both indenters, hardness increases with indentation depth, as expected; and second, hardness values for R = 550 nm are much higher than those for R = 3.3 μm. Swadener et al.[38] experimentally demonstrated that the difference in hardness for the different spheres are not by a surface effect (such as friction and surface layer) but by the indentation size effect (ISE) for sphere; the smaller the sphere, the higher the hardness. Similar observations have been

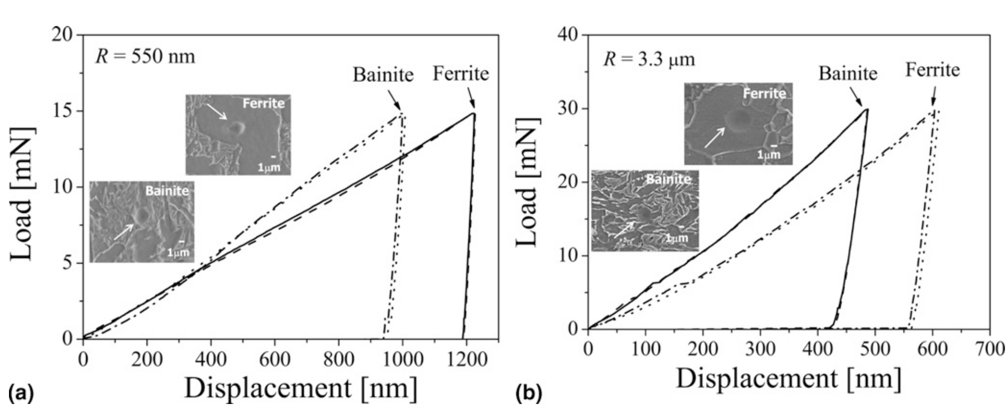

FIG. 2. Representative P-h curve recorded during nanoindentation on each phase with a spherical tip having a radius of (a) 550 nm and (b) 3.3 μm. Two curves obtained from the same target phase are almost overlapped, implying high reproducibility of the testing results.

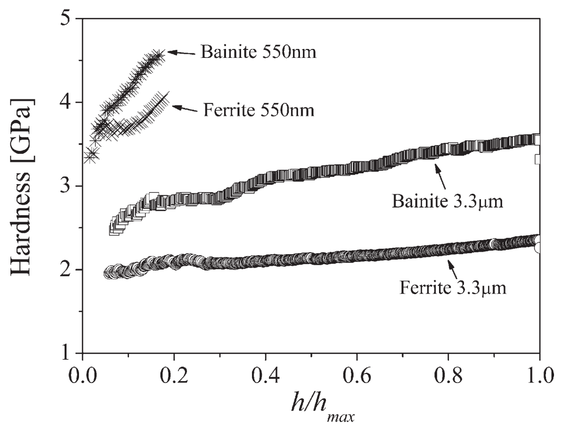

FIG. 3. Variation in hardness as a function of normalized indentation depth.

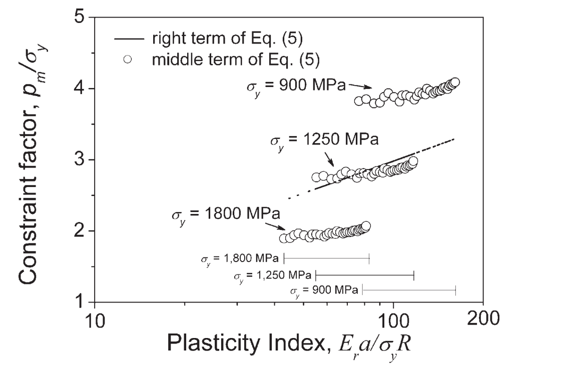

FIG. 4. An example presenting how to determine the yield strength for calculating the constraint factor (C).

reported by many researchers [for example, see Refs. 39–41]. We will return to this ISE issue later.

B. Estimating representative stress-strain of microphases

To estimate representative flow stress from the measured H by using Eq. (1), the constraint factor (C) still needs to be determined. Unlike sharp indentation, spherical indentation can undergo three distinct deformation regimes: elastic, elastic-plastic, and fully plastic regime. Johnson[36] showed that the indentation pressure under each deformation regime may be correlated on a graph of the C as a function of nondimensional plasticity index ($E_r \tan\beta/\sigma_y$), where E_r is the reduced modulus (determined from Young's modulus E and Poisson's ratio v of the specimen and the indenter),[16,17] σ_y is the yield strength, and β is the inclination of indenter to the surface.

According to Johnson's model,[42] whereas the C for the fully plastic deformation regime is approximately constant as 3, the relation between the C and the plasticity index for elastic-plastic regime can be described as:

$$C = \frac{p_m}{\sigma_y} = \frac{2}{3}[2 + \ln(\frac{(E_r/\sigma_y)\tan\beta + 4(1-2v)}{6(1-v)})] \quad . \quad (5)$$

For spherical indentation, $\tan\beta$ ($\approx\sin\beta$) can be replaced by a/R. In Eq. (5), whereas we simply adopted the well known elastic properties of steel, E = 210 GPa and ν = 0.3, σ_y values for each microphase were determined in the following iterative way. First, we put an arbitrary value of σ_y into both the middle term (P_m/σ_y) and the right term of Eq. (5). If the calculated value of the middle term (based on the measured H) is largely different from that of the right term, we varied the input value of σ_y. This procedure is repeated until both values become similar, and the most similar value of σ_y was applied to Eq. (5). An example of this procedure (for ferrite phase and R = 550 nm) is seen in Fig. 4. It is noteworthy that high values of obtained σ_y (1250 MPa in Fig. 4) may be partly due to the indentation size effect for yield stress. Recently, Zhu et al. reported that there might be a significant size effect in σ_y for spherical indentation.[43,44] Based on the assumption that the elastic-plastic regime ends and fully plastic regime begins at C = 3, if the value of C calculated by Eq. (5) is higher than 3, we used the value of 3 instead of the calculated value. For R = 3.3 μm, the obtained value of the plasticity index ($E_r\ a/\sigma_y R$) corresponding to C = 3 are approximately 100 for both phases, whereas the plasticity index value for R = 550 nm is approximately 100 and 80 for bainite and ferrite phase, respectively.

With the calculated representative stress and strain of each microphase, the plastic flow (i.e., relation between true stress and true strain) of each phase could be estimated by applying the following power-law relation (often referred to as Swift's equation[45]):

$$\sigma = A(B + \varepsilon)^n \quad , \quad (6)$$

where A is strength coefficient, B is strain-correction factor, and n is work-hardening exponent. Although the Swift's equation[45] is a hardening rule only slightly modified from popular Hollomon's work-hardening equation ($\sigma = A\varepsilon^n$),[46] it was reported in the literature[47,48] that the former better describes the work hardening of API pipeline steels than the latter.

Figure 5 shows the estimated plastic flow of each phase with elastic regime schematically drawn by putting E = 210 GPa into Hooke's law ($\sigma = E\ \varepsilon$). The figure suggests two clear trends in the change in stress value. First, as expected, the stress value of bainite phase at a given strain is much higher than that of ferrite. Second, there is a dependency of stress on indenter radius due to the indentation size effect (ISE) for sphere, as mentioned previously. Thus, the size effect should be taken into account when converting the nanoindentation data to proper macroscopic values. Following the well known ISE model by Nix and Gao,[49] Swadener et al.[38]

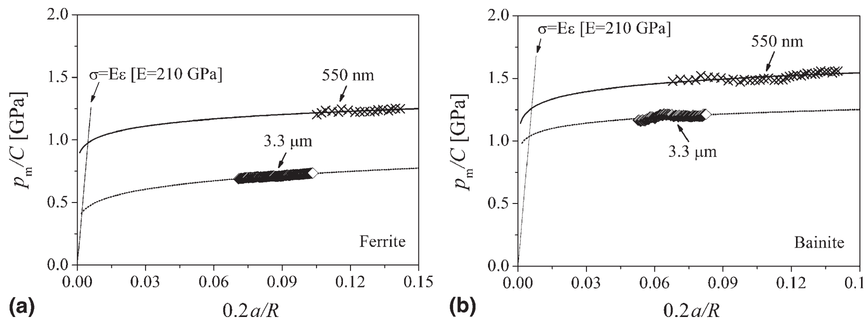

FIG. 5. Microscopic plastic flow curves of microphases derived from nanoindentation data; (a) ferrite and (b) bainite.

experimentally verified that, for spherical indentation, the indenter radius rather than indentation depth determines the indentation size effect according to the following equation:

$$H = H_0\sqrt{1 + \frac{R^*}{R}} \quad , \tag{7}$$

where H_o is the macroscopic hardness and R^* is a material length scale for the radius dependence of hardness. H and H_o can be simply replaced by σ and σ_o (the macroscopic stress) according to Eq. (1). Using the linear relation between σ and R^2, we derived the macroscopic plastic flow of each phase in a simple way; the stress values at four different plastic strains (ε = 0.08, 0.1, 0.12, and 0.14) from the plastic curves in Fig. 5 were fit linearly with two R^2 values (for 550 nm and 3.3 μm), and hence the macroscopic stress values were estimated by extrapolating the fitting line to R = 500 μm. The stress values at low plastic strain regime were not used for this estimation, due to the absence of available experimental data in the range (see Fig. 5). The reason why we applied σ values in Fig. 5 (instead of H values in Fig. 3) to Eq. (7) is that the ranges of the representative indentation strain experimentally obtained with two indenters are not exactly overlapped [note that Eq. (7) is available at a given strain]. Using all of the results described above, the macroscopic stress-strain curve of each microphase was derived as shown in Fig. 6. Again, elastic regime in the figure was schematically drawn according to Hooke's law with E = 210 GPa.

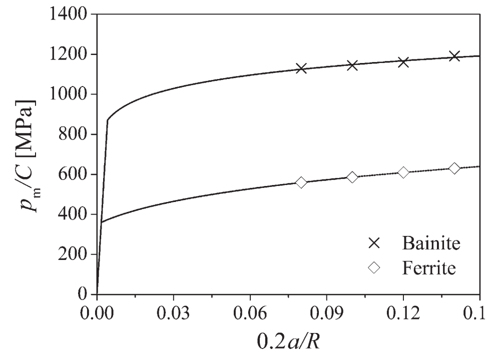

FIG. 6. Macroscopic flow stress-strain behavior of each phase.

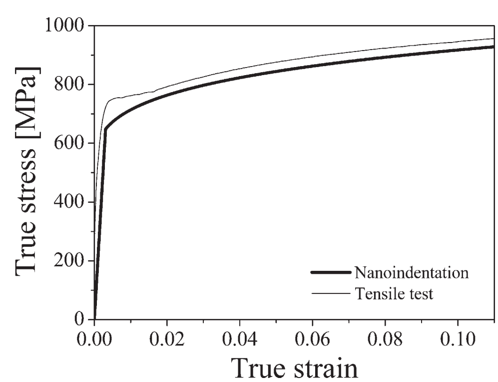

FIG. 7. Comparison of true stress-true strain curve extracted from nanoindentation experiments (on microphases) with that measured by the conventional tensile test (of a bulky sample).

C. Predicting macroscopic flow curve of dual-phase steel and its verification

Finally, with an assumption of isostrain at each phase, the macroscopic true stress for the dual-phase steel was predicted by applying a simple rule-of-mixture:

$$\sigma = \sigma_f V_f + \sigma_b V_b \quad , \tag{8}$$

where V is volume fraction and the subscriptions f and b indicate ferrite and bainite, respectively. As mentioned in Sec. II, V_f and V_b are approximately 41 and 59%, respectively, for the steel examined in present work. The flow stress σ_f and σ_b were taken, as shown in Fig. 6.

In Fig. 7, the macroscopic plastic flow curve derived from nanoindentation experiments is compared with that directly measured by conventional tensile test of a standard bulky sample. It can be seen that true stress versus true strain curves from both tests are in a reasonably good agreement; i.e., over a wide range of plastic strain, with the exception of the Lüders strain regime (that is clearly seen in the tensile curve but is not considered in the nanoindentation-based curve), the flow stresses from the tensile test are only approximately 30 MPa higher than that from nanoindentation tests. However, it is noteworthy that this difference in the stress can be increased if material pile-up around indentation (resulting in overestimation of hardness) is adequately considered. With the research objective in mind, we paid more attention to the predicted value of the work-hardening exponent (n), which might be one of the most important characteristics for "strain-based design" pipeline steels. Somewhat surprisingly, the exponent value from the tensile test ($n = 0.1156$) is close to that from nanoindentation tests ($n = 0.1175$). This implies that the deformability can be successfully predicted by performing spherical nanoindentation on the constituent microphases.

The slight difference in flow stress between two curves might arise from various factors we could not consider here. First, whereas we simply adopted the rule-of-mixture using matrix strength of each phase, the influence of grain (or phase) boundaries on the macroscopic strength was not considered in this work. However, high-angle grain (or phase) boundaries are known to induce strong strengthening. For instance, Jang et al.[50] experimentally demonstrated that the high-angle boundaries play an important role in the deformation during nanoindentation of structural steels. Second, because only two spherical indenters were used in this work, the relation of σ versus R^2 in Eq. (7) always fits perfectly as a single line, and thus the extrapolated macrostrength can be seriously affected by small fluctuation in σ (or H) value. Thus, the use of larger number of spherical indenters having different radii will certainly enhance the accuracy of predicted curve. If these factors would be additionally reflected into the procedure, more precise prediction of macroscopic strength from nanoindentation can be achieved, which might be useful in improving ability to design high-performance multiphase steel by optimizing volume fraction of constituent phases.

IV. CONCLUSION

To predict the macroscopic stress-strain curve of advanced high-performance pipeline steel consisting of dual constituent microphases (bainite and ferrite), nanoindentation experiments with two spherical indenters having different radii (550 nm and 3.3 μm) were performed on each phase. Popular concepts of indentation stress-strain and the indentation size effect were combined together to produce a simple procedure for extracting the true stress-true strain curve of each microphase (which cannot be obtained from conventional tensile tests). It was revealed that application of a simple rule-of-mixture using the strength values of each phase can lead to a reasonably successful prediction of macroscopic plastic flow of the dual-phase steel.

ACKNOWLEDGMENT

This work was sponsored by POSCO.

REFERENCES

1. N. Sanderson, R.K. Ohm, and M. Jacobs: Study of X100 linepipe costs point to potential saving. *Oil Gas J.* **97,** 54 (1999).
2. A. Glover, J. Zhou, D. Horsley, N. Suzuki, S. Endo, and J. Takehara: Design, application and installation of an X100 pipeline, in *Proceeding of OMAE 2003* (22nd International Conference on Offshore Mechanics and Arctic Engineering, Cancun, Mexico,2003), Art. No. OMAE2003-37429.
3. N. Ishikawa, M. Okatsu, S. Endo, and J. Kondo: Design concept and production of high deformability linepipe, in *Proceeding of IPC 2006* (6th International Pipeline Conference, Calgary, Canada, 2006), Art. No. IPC2006-10240.
4. N. Ishikawa, S. Endo, and J. Kondo: High performance UOE linepipes. *JFE Technical Report* **7,** 20 (2006).
5. D-H. Seo, C-M. Kim, J-Y. Yoo, and K-B. Kang: Microstructure and mechanical properties of X80/X100 grade plate and pipes, in *Proceeding of ISOPE 2007* (7th International Offshore and Polar Engineering Conference, Lisbon, Portugal, 2007), p. 3301.
6. N. Suzuki and M. Toyoda: Critical compressive strain of linepipes related to workhardening parameters, in *Proceeding of OMAE 2002* (21st International Conference on Offshore Mechanics and Arctic Engineering, Oslo, Norway, 2002), Art. No. OMAE2003-28253.
7. N. Suzuki, R. Muraoka, A. Glover, J. Zhou, and M. Toyoda: Local buckling behavior of X100 linepipes, in *Proceeding of OMAE 2003* (22nd International Conference on Offshore Mechanics and Arctic Engineering, Cancun, Mexico, 2003), Art. No. OMAE2003-37145.
8. S. Endo and M. Nagae: Ferrite-martensite dual phase anti-erosion steel. *ISIJ Int.* **36,** 95 (1996).
9. T. Hüper, S. Endo, N. Ishikawa, and K. Osawa: Effect of volume fraction of constituent phase on the stress-strain relationship of dual phase steels. *ISIJ Int.* **39,** 288 (1999).
10. Y. Tomota and I. Tamura: Mechanical behavior of steels consisting of two ductile phases. *Trans. ISIJ* **22,** 665 (1982).
11. Y. Tomota, M. Umemoto, N. Komatsubara, A. Hiramatsu, N. Nakajima, A. Moriya, T. Watanabe, S. Nanba, G. Anan, K. Kunishige, Y. Higo, and M. Miyahara: Prediction of mechanical properties of multi-phase steels based on stress-strain curve. *ISIJ Int.* **32,** 343 (1992).
12. Rudiono and Y. Tomota: Application of the secant method to prediction of flow curves in multi-microstructure steels. *Acta Mater.* **45,** 1923 (1997).
13. P.J. Jacques, J. Ladriere, and F. Delannay: On the influence of interactions between phases on the mechanical stability of retained austenite in transformation-induce plasticity multiphase steels. *Metall. Mater. Trans. A* **32,** 2759 (2001).
14. P.J. Jacques, Q. Furnémont, F. Lani, T. Pardoen, and F. Delannay: Multiscale mechanics of TRIP-assisted multiphase steels: I. Characterization and mechanical testing. *Acta Mater.* **55,** 3681 (2007).
15. F. Lani, Q. Furnémont, T. Van Rompaey, F. Delannay, P.J. Jacques, and T. Pardoen: Multiscale mechanics of TRIP-assisted multiphase steels: II. Micromechanical modeling. *Acta Mater.* **55,** 3695 (2007).
16. W.C. Oliver and G.M. Pharr: An improved technique for determining hardness and elastic modulus using load and displacement sensing indentation experiments. *J. Mater. Res.* **7,** 1564 (1992).
17. W.C. Oliver and G.M. Pharr: Measurement of hardness and elastic modulus by instrumented indentation: Advances in understanding and refinements to methodology. *J. Mater. Res.* **19,** 3 (2004).
18. Y-T. Cheng and C-M. Cheng: Scaling, dimensional analysis, and indentation measurements. *Mater. Sci. Eng., R* **44,** 91 (2004).
19. N.X. Randall, C. Julia-Schmutz, J.M. Soro, J. von Stebut, and G. Zacharie: Novel nanoindentation method for characterising multiphase materials. *Thin Solid Films* **308–309,** 297 (1997).

20. M. Göken and M. Kempf: Microstructural properties of superalloys investigated by nanoindentations in an atomic force microscope. *Acta Mater.* **47,** 1043 (1999).
21. Y. Choi, W.Y. Choo, and D. Kwon: Analysis of mechanical property distribution in multiphase ultra-fine-grained steels by nanoindentation. *Scr. Mater.* **45,** 1401 (2001).
22. Q. Furnémont, M. Kempf, P.J. Jacques, M. Göken, and F. Delannay: On the measurement of the nanohardness of the constitutive phases of TRIP-assisted multiphase steels. *Mater. Sci. Eng., A* **328,** 26 (2002).
23. G.B. Viswanathan, E. Lee, D.M. Maher, S. Banerjee, and H.L. Fraser: Direct observation and analyses of dislocation substructures in the α phase of an α/β Ti-alloy formed by nanoindentation. *Acta Mater.* **53,** 5101 (2005).
24. M. Delincé, P.J. Jacques, and T. Pardoen: Separation of size-dependent strengthening contribution in fine-grained Dual Phase steels by nanoindentation. *Acta Mater.* **54,** 3395 (2006).
25. D. Tabor: *Hardness of Metals* (Clarendon Press, Oxford, UK, 1951).
26. K.L. Johnson: *Contact Mechanics* (Cambridge Univ. Press, Cambridge, UK, 1985).
27. J.S. Field and M.V. Swain: A simple predictive model for spherical indentation. *J. Mater. Res.* **8,** 297 (1993).
28. J.G. Swadener, B. Taljat, and G.M. Pharr: Measurement of residual stress by load and depth-sensing indentation with spherical indenters. *J. Mater. Res.* **16,** 2091 (2001).
29. A.G. Atkins and D. Tabor: Plastic indentation in metals with cones. *J. Mech. Phys. Solids* **13,** 149 (1965).
30. Y.V. Milman, B.A. Galanov, and S.I. Chugunova: Plasticity characteristic obtained through hardness measurement. *Acta Metall. Mater.* **41,** 2523 (1993).
31. S. Jayaraman, G.T. Hahn, W.C. Oliver, C.A. Rubin, and P.C. Bastias: Determination of monotonic stress-strain curve of hard materials from ultra-low-load indentation tests. *Int. J. Solids Struct.* **35,** 365 (1998).
32. S. Shim, J-I. Jang, and G.M. Pharr: Extraction of flow properties of single-crystal silicon carbide by nanoindentation and finite element simulation. *Acta Mater.* **56,** 3823 (2008).
33. H. Hertz: *Miscellaneous Papers*, edited by D.E. Jones and G.H. Schott (Macmillan, London, 1896).
34. E.G. Herbert, W.C. Oliver, and G.M. Pharr: On the measurement of yield strength by spherical indentation. *Philos. Mag.* **86,** 5521 (2006).
35. J-I. Jang, Y. Choi, J-S. Lee, Y-H. Lee, D. Kwon, M. Gao, and R. Kania: Application of instrumented indentation technique for enhanced fitness-for-service assessment of pipeline crack. *Int. J. Fract.* **131,** 15 (2005).
36. Y.P. Cao and J. Lu: A new method to extract the plastic properties of metal materials from an instrumented spherical indentation loading curve. *Acta Mater.* **52,** 4023 (2004).
37. A. Sreeranganathan, A. Gokhale, and S. Tamirisakandala: Determination of local constitutive properties of titanium alloy matrix in boron-modified titanium alloys using spherical indentation. *Scr. Mater.* **58,** 114 (2008).
38. J.G. Swadener, E.P. George, and G.M. Pharr: The correlation of the indentation size effect measured with indenters of various shapes. *J. Mech. Phys. Solids* **50,** 681 (2002).
39. Y.Y. Lim and M.M. Chaudhri: The effect of the indenter load on the nanohardness of ductile metals: An experimental study on polycrystalline work-hardened and annealed oxygen-free copper. *Philos. Mag.* **79,** 2979 (1999).
40. I.J. Spary, A.J. Bushby, and N.M. Jennett: On the indentation size effect in spherical indentation. *Philos. Mag.* **86,** 5581 (2006).
41. K. Durst, M. Göken, and G.M. Pharr: Indentation size effect in spherical and pyramidal indentations. *J. Phys. D: Appl. Phys.* **41,** 074005 (2008).
42. K.L. Johnson: The correlation of indentation experiments. *J. Mech. Phys. Solids* **18,** 115 (1970).
43. T.T. Zhu, A.J. Bushby, and D.J. Dunstan: Size effect in the initiation of plasticity for ceramics in nanoindentation. *J. Mech. Phys. Solids* **56,** 1170 (2008).
44. T.T. Zhu, X.D. Hou, A.J. Bushby, and D.J. Dunstan: Indentation size effect at the initiation of plasticity for ceramics and metals. *J. Phys. D: Appl. Phys.* **41,** 074004 (2008).
45. H.W. Swift: Plastic instability under physics of solids. *J. Mech. Phys. Solids* **1,** 1 (1952).
46. J.H. Hollomon: Tensile deformation. *Trans. AIME* **162,** 268 (1945).
47. Y.M. Kim, S.K. Kim, Y.J. Lim, and N.J. Kim: Effect of microstructure on the yield ratio and low temperature toughness of linepipe steels. *ISIJ Int.* **42,** 1571 (2002).
48. S.K. Kim, Y.M. Kim, Y.J. Lim, and N.J. Kim: Relationship between yield ratio and the material constant of the swift equation. *Met. Mater. Int.* **12,** 131 (2006).
49. W.D. Nix and H. Gao: Indentation size effects in crystalline materials: A law for strain gradient plasticity. *J. Mech. Phys. Solids* **46,** 411 (1998).
50. J-I. Jang, S. Shim, S. Komazaki, and T. Honda: A nanoindentation study on grain-boundary contributions to strengthening and aging degradation mechanisms in advanced 12 Cr ferritic steel. *J. Mater. Res.* **22,** 175 (2007).